



OPTICS

NeuWS: Neural wavefront shaping for guidestar-free imaging through static and dynamic scattering media

Brandon Y. Feng^{1†}, Haiyun Guo^{2†}, Mingyang Xie¹, Vivek Boominathan², Manoj K. Sharma², Ashok Veeraraghavan^{2‡*}, Christopher A. Metzler^{1‡*}

Diffraction-limited optical imaging through scattering media has the potential to transform many applications such as airborne and space-based imaging (through the atmosphere), bioimaging (through skin and human tissue), and fiber-based imaging (through fiber bundles). Existing wavefront shaping methods can image through scattering media and other obscurants by optically correcting wavefront aberrations using high-resolution spatial light modulators—but these methods generally require (i) guidestars, (ii) controlled illumination, (iii) point scanning, and/or (iv) statics scenes and aberrations. We propose neural wavefront shaping (NeuWS), a scanning-free wavefront shaping technique that integrates maximum likelihood estimation, measurement modulation, and neural signal representations to reconstruct diffraction-limited images through strong static and dynamic scattering media without guidestars, sparse targets, controlled illumination, nor specialized image sensors. We experimentally demonstrate guidestar-free, wide field-of-view, high-resolution, diffraction-limited imaging of extended, nonsparse, and static/dynamic scenes captured through static/dynamic aberrations.

INTRODUCTION

Diffraction-limited optical imaging is a fundamental goal across a range of fields, from astronomy and remote sensing to biology and medical imaging. Optical aberrations, such as turbulence and scattering, represent the central impediments to this goal (1–3). Accordingly, imaging through severe time-varying aberrations and scattering media has been repeatedly identified as one of the most important open problems in optics (2, 3).

Existing methods for imaging through scattering media are limited in multiple ways: They (i) require guidestars, (ii) require point by point scanning, (iii) use illumination control, and (iv) cannot handle dynamics in either the scattering media or the subject being imaged. Adaptive optics (AO) is arguably the most popular technique used to compensate for optical aberrations (4, 5). However, the limited degrees of freedom in deformable mirror arrays (generally under 1000) limits AO to correcting only lower-order aberrations. In addition, most traditional AO methods require guidestars. Digital AO methods, which simultaneously estimate both optical aberrations and the corresponding aberration-free scenes using lightfield measurements, are similarly limited to lower-order aberrations (6, 7).

Wavefront shaping (WS) techniques can correct for higher-order aberrations like scattering using high-resolution spatial light modulators (SLMs), which have tens of thousands to millions of degrees of freedom (8, 9). However, to date, most WS methods either assume that the scene contains fluorescent (10–12), photoacoustic (13), acousto-optic (14), or nonlinear (15, 16) guidestars or assume that one can measure the aberration beforehand (17, 18). Meanwhile, passive and purely computationally techniques, like

speckle correlation imaging (19–23), make strong assumptions about the distribution of the aberrations and are limited to reconstructing sparse and simple scenes. Recently developed optical computing techniques are similarly limited to simple scenes and assume that the distribution of the aberrations is known (24).

Building off methods first designed to focus light within scattering media (25–28), a recent breakthrough technique, imaged-guided WS (IGWS) (29), demonstrated guidestar-free WS-based imaging through scattering media. However, IGWS requires adaptively capturing tens to hundreds of thousands of images (acquired over hours), greatly restricting its practical utility.

Here, we introduce neural WS (NeuWS), a WS technique that can computationally correct for severe time-varying isoplanatic aberrations without a guidestar. Our method poses wavefront sensing as a maximum likelihood estimation problem and then relies on time-varying neural signal representations to jointly estimate the optical aberration's phase and the object of interest's brightness. This formulation regularizes the associated optimization problem and allows us to efficiently leverage temporal regularity in the data, without restricting ourselves to static objects and aberrations.

By combining estimation theory with neural representations, NeuWS offers an unprecedented set of capabilities: Noninvasively and without illumination control, we experimentally demonstrate postcapture, guidestar-free, wide-field, high-resolution, diffraction-limited imaging of extended, nonsparse, and dynamic scenes through severe time-varying optical aberrations.

RESULTS

The goal of AO and WS is to manipulate an aberrated wavefront so as to counteract the aberration and form a diffraction-limited image. Existing image-guided AO and WS search for a wavefront correction that maximizes some image quality metric (30), such as sharpness (31–33), the power in particular frequency bands (34), variance (26, 28), or entropy (29). These image quality

¹Department of Computer Science, The University of Maryland, College Park, College Park, MD 20742, USA. ²Department of Electrical and Computer Engineering, Rice University, Houston, TX 77005, USA.

*Corresponding author. Email: vashok@rice.edu (A.V.); metzler@umd.edu (C.A.M.)

†These authors contributed equally to this work.

‡These authors contributed equally to this work.

Copyright © 2023 The Authors, some rights reserved; exclusive licensee American Association for the Advancement of Science. No claim to original U.S. Government Works. Distributed under a Creative Commons Attribution NonCommercial License 4.0 (CC BY-NC).

Downloaded from https://www.science.org at University of Maryland College Park on June 06, 2024

metrics are hand-chosen and reflect a priori on what the aberration-free image should look like. Accordingly, existing image-guided AO and WS methods are inherently heuristic.

By contrast, NeuWS treats aberration correction as an estimation problem and seeks statistically optimal estimates of both the phase of the optical aberration and the brightness of the object of interest. To do so, NeuWS captures a series of modulated measurements and uses these measurements to form maximum likelihood estimates of each quantity.

A schematic of NeuWS is presented in Fig. 1A. An incoherently illuminated object is imaged by our optical system, which has an unknown optical aberration at its aperture plane. Taking inspiration from coded diffraction pattern phase retrieval (35) and computational wavefront sensing (17, 36, 37), a series of known and stochastically generated patterns $\Gamma_1, \Gamma_2, \dots, \Gamma_L$ are displayed on a phase-only SLM, which is imaged onto the system's aperture plane with a $4f$ system. Example modulation patterns and their corresponding measurements are presented in Fig. 1C. Under the assumption

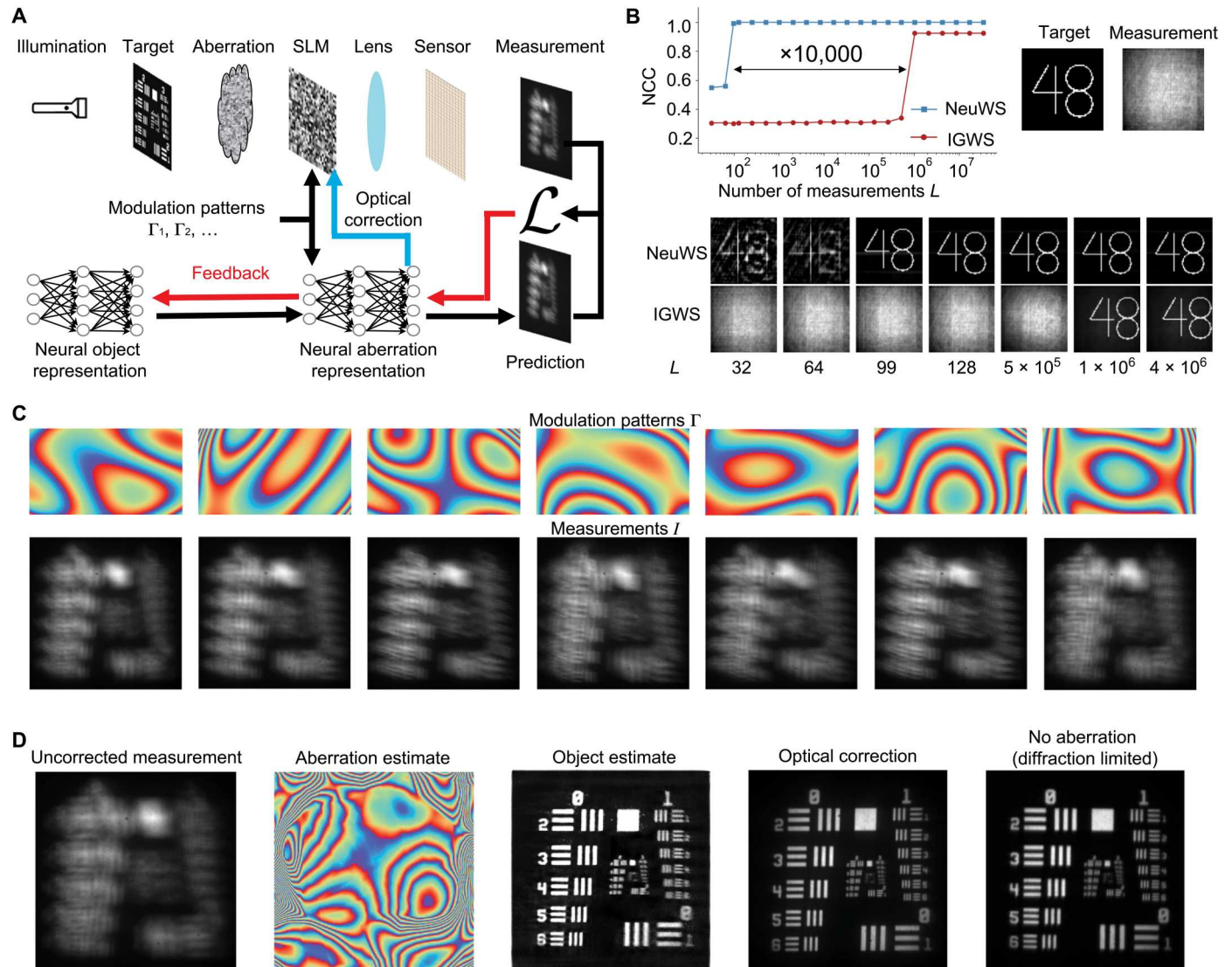


Fig. 1. NeuWS operating principles, comparisons, and experimental demonstration. (A) Neural wavefront shaping (NeuWS) images a high-resolution SLM onto the surface of an optical aberration (e.g., soft tissue). The spatial light modulator (SLM) modulates the aberrated light with a sequence of randomly generated patterns $\Gamma_1, \dots, \Gamma_L$, and the light is then Fourier-transformed by a lens onto a sensor. The captured images are compared with images simulated using a neural network-based model of the optical system, and backpropagation is used to estimate the target and aberration, thereby computationally correcting for the aberration. The conjugate of the estimated aberration phase error can be displayed on the SLM to optically correct for the aberration. (B) Comparison between NeuWS and image-guided WS (IGWS) (29). Both are tasked with correcting for scattering-induced optical aberrations (simulated with complex circular Gaussian wavefront errors) using a varied number of total measurements. Reconstruction quality is measured by normalized correlation coefficient (NCC). NeuWS can correct for optical aberrations using orders of magnitude fewer measurements. (C) Example of phase modulation patterns Γ displayed on the SLM (top) and the corresponding measurement that each pattern produces (bottom). (D) Experimental reconstructions of a negative USAF resolution target imaged through a glass slide covered in nail polish. NeuWS produces accurate digital reconstructions of the aberration (aberration estimate) and the object (object estimate) using 30 measurements, such as those shown in (C). Optical correction denotes an image captured with the conjugate of the aberration estimate displayed on the SLM. No aberration denotes an image captured without an aberration along the optical path.

that the optical aberrations are isoplanatic and the illumination is spatially incoherent and monochromatic, this procedure results in a sequence of measurements described by

$$I_i = O_o * H_i + Z_i \text{ with } H_i = |\mathcal{F}[M \circ e^{j(\Phi_o + \Gamma_i)}]|^2 \quad (1)$$

where I_i denotes the i th observation, H_i denotes the i th point spread function, O_o denotes the brightness of the object of interest, \mathcal{F} denotes the two-dimensional (2D) Fourier transform, Φ_o denotes the phase of the optical aberration (which can include defocus), M denotes the known binary mask/pupil defined by the shape of the aperture, and Z_i denotes the i th realization of noise. If the elements of all Z_i follow independent identically distributed Gaussian distributions, then, up to constants, the negative log likelihood of

the measurements, $-\ln p(I_1, \dots, I_L | O, \Phi)$, is proportional to

$$\mathcal{L}_{\text{static}}(O, \Phi) = \sum_{i=1}^L \|I_i - O * |\mathcal{F}[M \circ e^{j(\Phi + \Gamma_i)}]|^2\|^2 \quad (2)$$

One could minimize the loss from Eq. 2 with respect to Φ and O to form maximum likelihood estimates of the true wavefront error and object brightness, Φ_o and O_o . However, as we demonstrate in the Supplementary Materials, the negative log-likelihood loss function is too nonconvex for this direct approach to be effective, and the optimization becomes stuck in inaccurate local minima.

In this work, we regularize the estimation problem by parameterizing Φ and O as the output of two untrained coordinate-based neural networks, $\phi(u, v): \mathbb{R}^2 \rightarrow [0, 2\pi]$ and $o(x, y): \mathbb{R}^2 \rightarrow \mathbb{R}_{\geq 0}$. These networks, which rely on no external training data, map 2D spatial coordinates (u, v) and (x, y) to estimates of the aberration and object brightness, respectively. One can form Φ and O by evaluating ϕ and

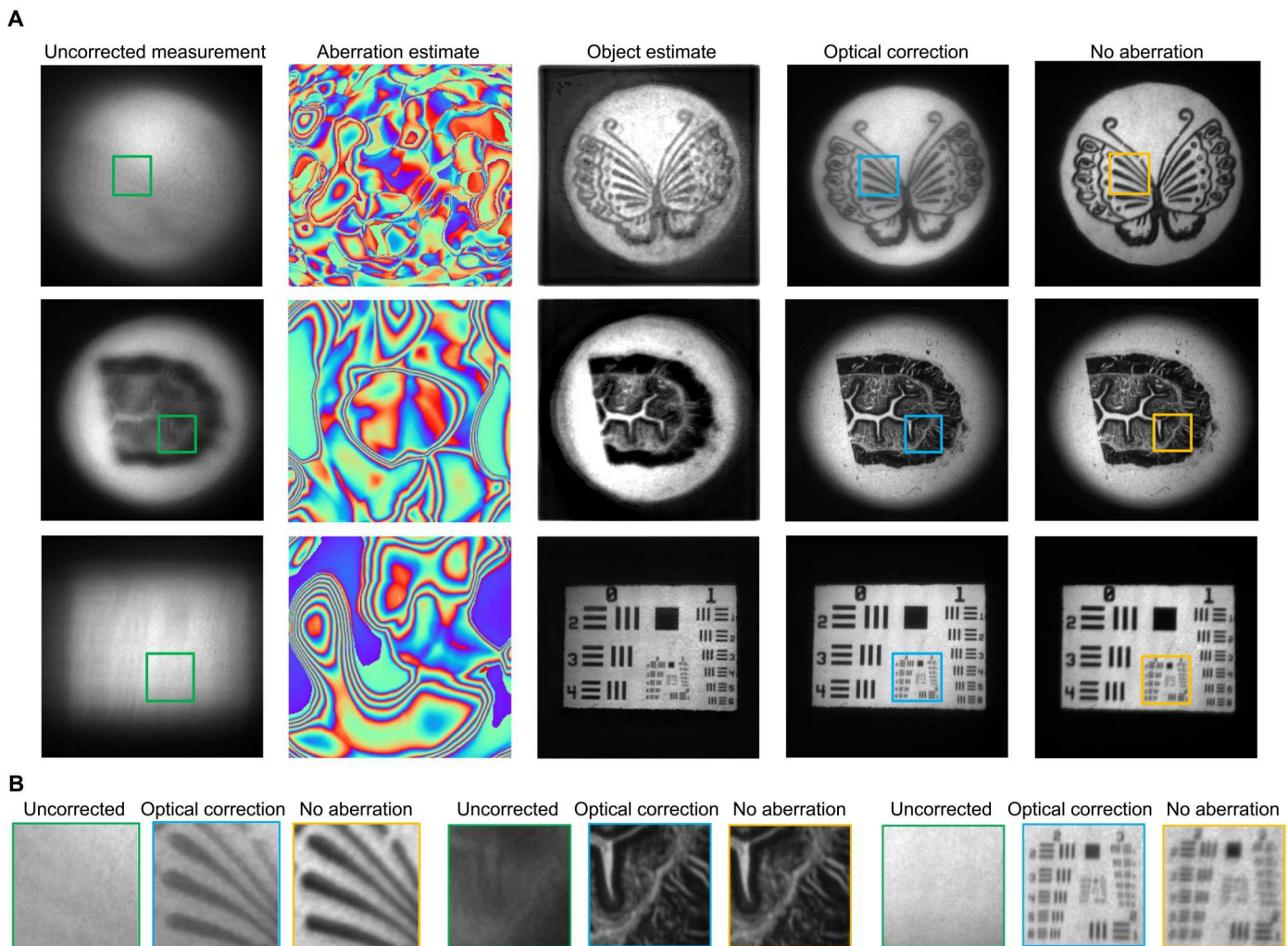


Fig. 2. Imaging static objects through static aberrations. (A) Experimental results of imaging a butterfly stamp through $\sim 80 \mu\text{m}$ of onion skin using 500 measurements (top), a dog esophagus tissue sample through a 0.5° diffuser using 100 measurements (middle), and a positive resolution target through a glass slide covered in nail polish using 100 measurements (bottom). (B) Close-ups of the uncorrected images (green), the optically corrected images (blue), and the reference images (orange) captured without an aberration in the optical path. NeuWS successfully corrects all three optical aberrations.

o at all (u, v) and (x, y) on a pixel grid. Φ and O can then be used to compute the loss defined by Eq. 2.

Such coordinate-based neural representations are inherently continuous and treat images as functions, rather than matrices. They excel at parsimoniously representing complicated signals, they do not explicitly restrict the reconstructions to a subspace (e.g., Zernike basis), and they can quickly pick up on and reinforce regularity in the data (38). As demonstrated in the Supplementary Materials, the negative log-likelihood loss landscape defined by Eq. 2 is far smoother and easier to optimize when parameterized as a function of the neural representation weights, rather than pixel values or Zernike coefficients. This regularity allows us to efficiently optimize o and ϕ using stochastic gradient descent, starting from random initializations. Related network-based parameterizations of images have been applied successfully to microscopy (39, 40), tomographic microscopy (41, 42), magnetic resonance imaging (43), and other applications (44–50).

A major advantage of NeuWS's estimation theory-based approach to WS is that it markedly reduces the number of measurements required to correct a wavefront error. Figure 1B compares the reconstruction accuracy of NeuWS and IGWS (29). Both are tasked with recovering an image of the number "48" through a simulated thin scattering media (every pixel of the simulated wavefront error follows an independent and identically distributed complex circular Gaussian distribution, introducing both amplitude and phase errors). NeuWS can accurately recover the object using 10,000× fewer measurements: 100 instead of 100,000. Comprehensive comparisons with IGWS (29) are provided in the Supplementary Materials.

In all figures shown here, "uncorrected" denotes images captured through an unknown optical aberration, "object estimate" denotes NeuWS's estimates (O) of each object's brightness, "aberration estimate" denotes NeuWS's estimates (Φ) of each aberration's phase error, "optical correction" denotes images captured after compensating for aberrations by displaying the conjugate ($-\Phi$) of each aberration estimate on the SLM, and "no aberration" denotes images captured without an optical aberration (e.g., chicken breast tissue) in the optical path.

Imaging static objects through static aberrations

We first validated the NeuWS framework by using it to image static objects through static aberrations. Our results are summarized in Fig. 2. We imaged a stamp of a butterfly, a prepared tissue sample of a dog esophagus, and a positive United States Air Force resolution target through aberration layers made, respectively, of onion skin, a 0.5° optical diffuser, and a glass slide coated with dried nail polish. For the butterfly stamp, we captured 500 modulated measurements, and for the other two samples, we captured 100 modulated measurements each. We also captured reference images of the target objects without any aberrations present.

Given this dataset, we minimized the negative log-likelihood loss from Eq. 2 to estimate the wavefront aberrations and the object brightness. We also displayed the conjugate of the aberration estimate on our SLM to optically correct for the aberration. As shown in Fig. 2B, NeuWS's optically corrected images match the resolution of the aberration-free images.

Imaging dynamic objects through static aberrations

Dynamic objects present a challenge for existing image-guided AO and WS methods. These methods estimate wavefront corrections using feedback provided by an image quality metric. If object movement causes this metric to change, then it will provide an erroneous feedback signal that can push the correction away from the truth.

One of the biggest strengths of NeuWS is that it can be easily extended to handle time-varying optical systems. To do so, one merely modifies the negative log likelihood and neural representations to model time-varying measurements. The negative log-likelihood loss becomes, up to constants, proportional to

$$\mathcal{L}_{\text{dynamic}}[O(t_i), \Phi(t_i)] = \sum_{i=1}^L \|I(t_i) - O(t_i) * \mathcal{F}\{M \circ e^{j[\Phi(t_i) + \Gamma_i]}\}\|^2 \quad (3)$$

where $I(t_i)$, $O(t_i)$, and $\Phi(t_i)$ are time-indexed representations of the image, object, and phase error. The neural representations of Φ and O similarly become $\phi(u, v, t): \mathbb{R}^3 \rightarrow [0, 2\pi]$ and $o(x, y, t): \mathbb{R}^3 \rightarrow \mathbb{R}_{\geq 0}$. Such representations, which treat the object and aberration as functions of both space and time, allow one to leverage temporal regularity in the data without having explicit models on the dynamics over time.

In our second set of experiments, we imaged a rotating stamp of a butterfly through approximately 400 μm of chicken breast and a rotating stamp of a fish through a 0.5° diffuser. The butterfly and fish stamps each rotated counterclockwise at 0.5° per frame. We captured 100 modulated measurements (one per angle) of the butterfly stamp and another 100 measurements (one per angle) of the fish stamp. We then minimized the time-varying log-likelihood loss (Eq. 3), where the object O (but not the aberration Φ) was parameterized as a function of time to form estimates of O and Φ . As demonstrated in Fig. 3, NeuWS can successfully estimate static aberrations while imaging dynamic objects, thereby allowing it to both computationally and optically correct for aberrations. Video reconstructions of these and other time-varying scenes can be found in the Supplementary Materials.

Imaging static objects through dynamic aberrations

Correcting dynamic aberrations represents an important and largely open challenge in WS (3). Guidestar-based methods have worked to address this problem by reducing system latency, so that they can measure and correct an aberration before it changes (51). Meanwhile, guidestar-free methods have so far restricted themselves to static aberrations (29).

In this work, we address the dynamic aberration challenge through computational wavefront correction. Rather than trying to push down system latency so that we can optically correct an aberration before it changes, we computationally correct for the wavefront error postcapture in the form of our object brightness estimate.

To validate our approach to removing time-varying optical aberrations, we imaged a static sample of rabbit testes cells and a static slide with two fingerprints through a rotating 0.5° diffuser and a rotating glass slide covered in nail polish, respectively. The diffuser rotated clockwise at 0.2° per frame, while the nail polished rotated clockwise at 0.5° per frame. We captured 50 modulated measurements of the rabbit cells and 30 modulated measurements of the

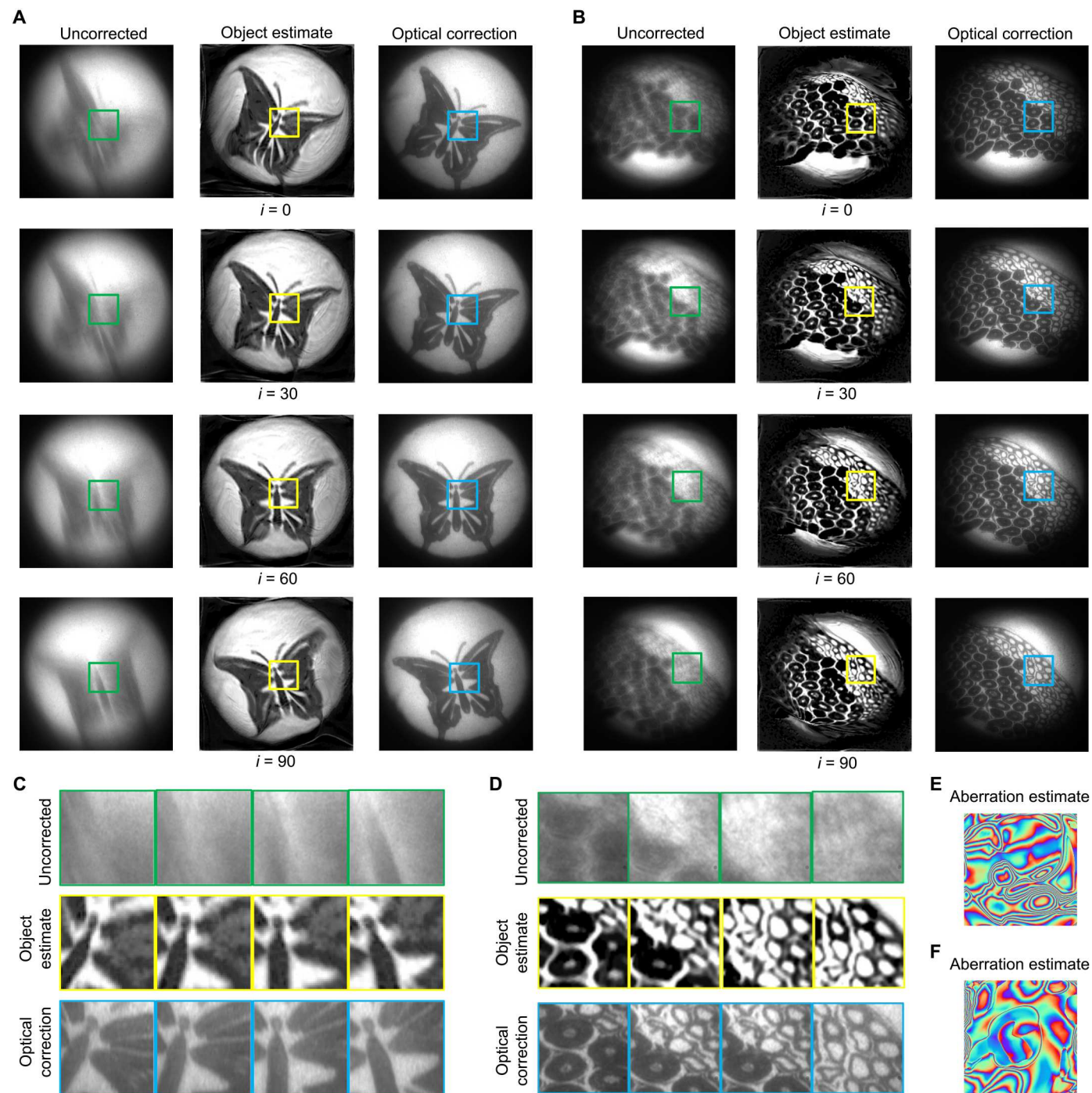


Fig. 3. Imaging dynamic objects through static aberrations. (A) Experimental results of imaging a rotating butterfly stamp through ~400 μm of chicken breast using 100 measurements. (B) Experimental results of imaging a moving fish stamp through a 0.5° diffuser using 100 measurements. (C and D) Close-ups of regions of interest of the butterfly and fish stamps. (E and F) Estimates of phase errors produced by the the chicken breast and the diffuser, respectively. NeuWS can successfully estimate static aberrations while imaging dynamic objects, thereby allowing it to both computationally and optically correct for aberrations.

fingerprints. We then estimated the object and aberration by minimizing the time-varying log-likelihood loss (Eq. 3), where the aberration (but not the object) was parameterized as a function of time. As demonstrated in Fig. 4, NeuWS can successfully estimate and thus computationally correct for time-varying optical aberrations. In the Supplementary Materials, we demonstrate that if one ignores the aberration dynamics and estimates a single static wavefront error for all measurements, then the reconstruction quality suffers severely.

Imaging dynamic objects through dynamic aberrations

Last, we used NeuWS to image dynamic objects through strong dynamic aberrations—a task well beyond the capabilities of existing guidestar-free WS techniques. In our experiments, we imaged rotating stamps of an owl and a turtle through translating aberrations made of onion skin ($\sim 80\ \mu\text{m}$ in thickness) and a 0.5° diffuser.

The owl stamp and turtle stamp were each rotated counterclockwise 0.5° per frame. At the same time, the onion and diffuser were translated $0.1\ \text{mm}$ per frame. We captured 100 modulated measurements (one per angle) of the owl stamp and another 100 modulated measurements (one per angle) of the turtle stamp. We then formed our object and aberration estimates by minimizing the time-varying loss from Eq. 3, with the aberration and object parameterized as functions of space and time. As demonstrated in Fig. 5, NeuWS can successfully reconstruct time-varying objects through time-varying optical aberrations. Features that are nearly invisible in the uncorrected images show up clearly in the object estimates.

We further validated the accuracy of our aberration estimates by performing optical correction. To do so, we rotated and translated the objects and aberrations back to their positions when each frame was captured. (In most applications, getting a wavefront error to repeat itself in such a manner is impractical or impossible.) We

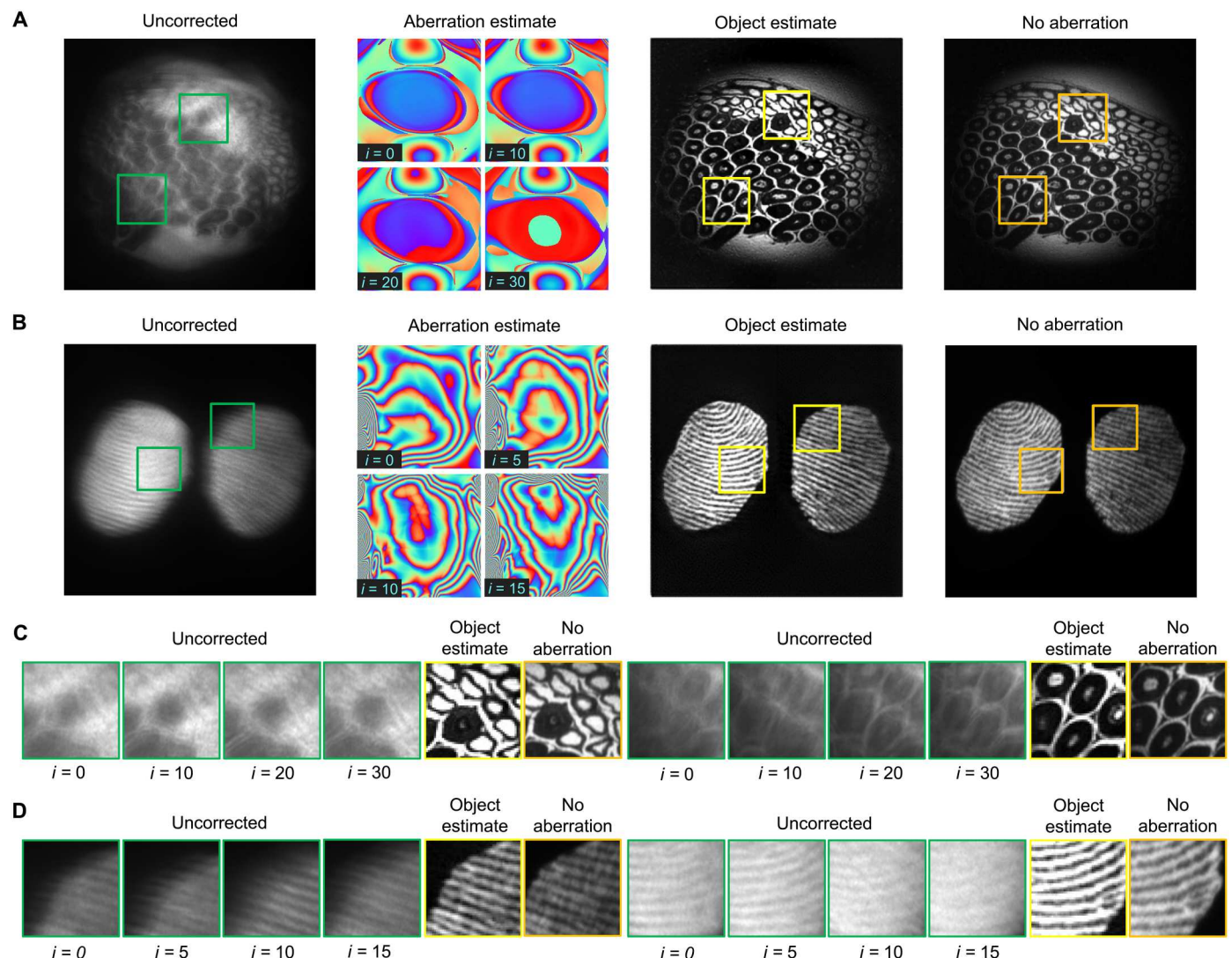


Fig. 4. Imaging static objects through dynamic aberrations. (A) Experimental results of imaging a static rabbit testes sample through a rotating 0.5° diffuser using 50 measurements. (B) Experimental results of imaging a static fingerprints slide through a rotating glass slide covered in nail polish using 30 measurements. (C and D) Close-ups of regions of interest of the rabbit sample and fingerprints, respectively. NeuWS can successfully estimate and thus computationally correct for time-varying optical aberrations.

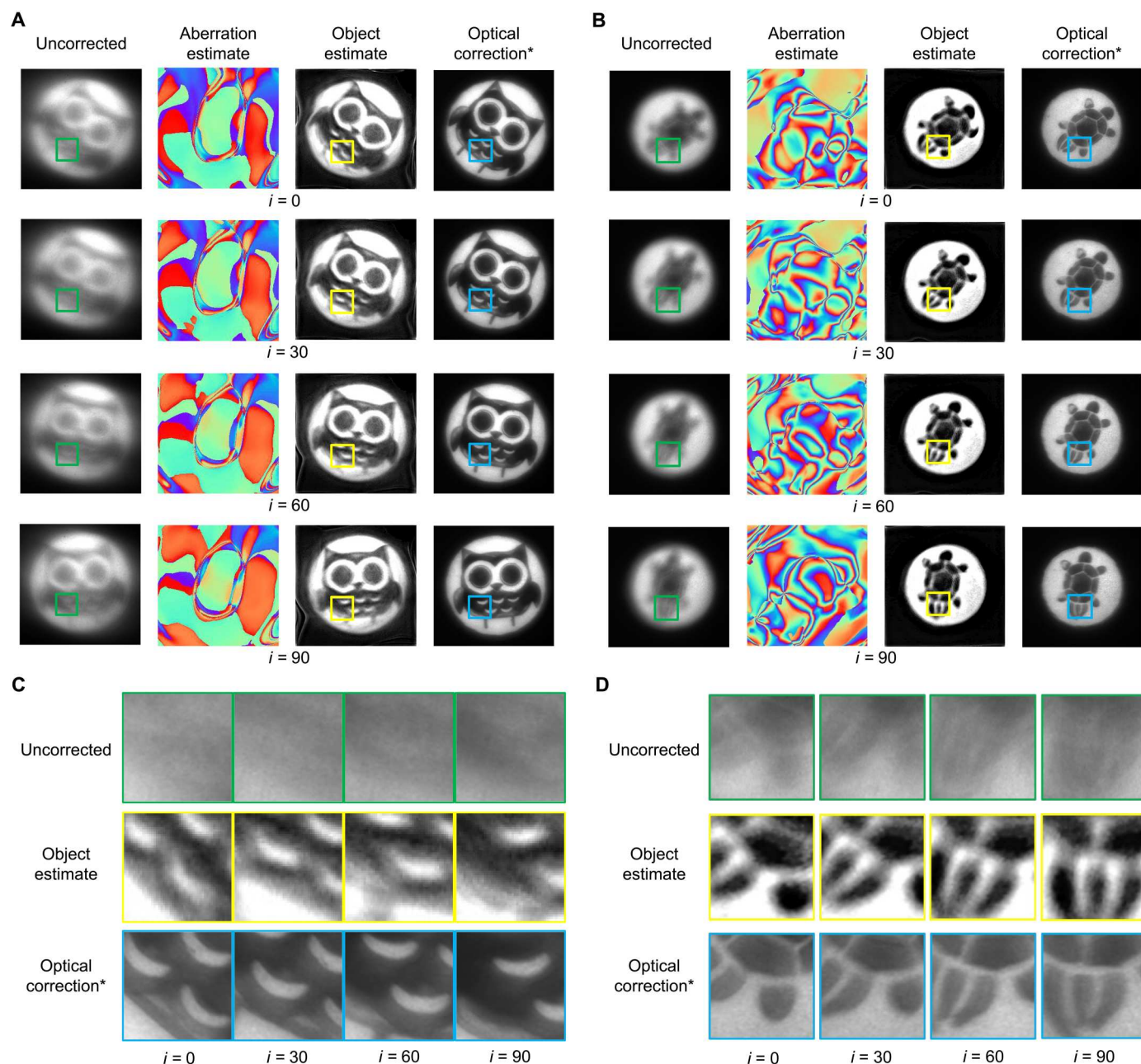


Fig. 5. Imaging dynamic objects through dynamic aberrations. (A) Experimental results of imaging a rotating owl stamp through $\sim 80 \mu\text{m}$ of translating onion skin using 100 measurements. (B) Experimental results of imaging a rotating turtle stamp through a translating 0.5° diffuser using 100 measurements. (C and D) Close-ups of regions of interest of (A) and (B), respectively. NeuWS can successfully reconstruct time-varying objects through time-varying optical aberrations. *In practice, optically correcting a time-varying aberration is only possible if one can estimate the aberration before it changes. In these experiments, we enabled optical correction by rotating and translating the object and aberration back to previously observed positions.

then used the SLM to apply the conjugate of the aberration estimates associated with each frame, producing excellent optical corrections of the data, as shown in Fig. 5.

DISCUSSION

NeuWS combines an estimation theory-based approach to WS with time-varying neural representations to enable high-resolution

guidestar-free WS through severe time-varying optical aberrations. In doing so, NeuWS provides a breakthrough set of capabilities that substantially advance what is possible with AO and WS.

NeuWS is a general-purpose approach to WS. It can correct for lower-order optical aberrations like defocus (see the Supplementary Materials) as well as higher-order aberrations, like scattering. It is not restricted to imaging only binary, sparse, or simple scenes. Its maximum resolution is diffraction limited by its aperture size, and

like other WS methods, in the presence of strong scattering, it can, in theory, enhance contrast by up to $\eta = \frac{\pi}{4}N$, where N is the number of controlled pixels in the SLM (8). Like many other WS techniques, NeuWS can only perform correction up to translation: Because they produce equivalent measurements, NeuWS cannot differentiate between tilts in the aberration's phase and translations of the object.

All optical WS techniques are plagued by latency: In any dynamic system, there is some amount of mismatch between the wavefront that was measured (the past) and the wavefront that the system is trying to optically correct (the present). Because in vivo aberration decorrelation times can be on the order of milliseconds (52), system latency represents a major barrier to optical WS. While the nascent field of predictive AO/WS may eventually provide a solution (53), it is not yet ready to fully address this challenge.

In the context of optical WS, the computational nature of NeuWS exacerbates the latency problem. With our current unoptimized implementation of NeuWS, estimating a 256-by-256 wavefront errors takes 1 to 20 min (depending on the number of measurements and whether the networks are parameterized as functions of time) on an NVIDIA 3090 RTX graphics processing unit. However, unlike other WS methods, NeuWS also estimates the aberration-free object. That is, even when NeuWS (or any other method) is too slow to optically correct the wavefront, NeuWS can perform computational WS postcapture. Because these corrections are performed postcapture on already collected data, NeuWS is able to sidestep the latency problem: The aberration that is computationally removed is (an estimate of) the aberration that was present when the measurements were captured. Thus, NeuWS can perform wavefront correction as quickly as it can modulate and capture images.

In our experiments, each image in the measurement sequences had an exposure time of 90 to 120 ms. In addition, between each modulated frame, we captured an unmodulated frame (they were not used during reconstruction and only served to visualize the aberrations). Thus, our experiments ran at roughly 5 Hz. Assuming that one is able to gather enough incoherent light, NeuWS's maximum framerate is determined by the minimum of the SLM refresh rate and the camera frame rate. In our current system, our SLM imposes a hard limit of 60 Hz. However, next-generation SLMs can operate at kilohertz rates—potentially fast enough to perform WS through thick living tissue.

Our proof-of-principle demonstrations were restricted to isoplanatic aberrations and planar scenes, which can be corrected with and put in focus by a single SLM pattern. In the context of imaging through scattering media, the isoplanatic aberration assumption corresponds to imaging within the memory effect region. While the theory behind NeuWS naturally extends to multiplanar aberration and object models, which could be corrected and imaged with multiconjugate AO, there remain notable computational and experimental challenges that must be overcome to put this into practice: The multiplanar forward model is no longer described by convolution, and one would need to align multiple SLMs to operate the system. Failed attempts to correct anisoplanatic aberrations with our current NeuWS implementation are presented in the Supplementary Materials.

Like other AO and WS methods, NeuWS is complementary to alternative scattering rejection/correction mechanisms, like two-photon microscopy (54), optical coherence tomography (55, 56), and time-of-flight imaging (57). Combining NeuWS with these and other imaging technologies is a promising avenue for future work.

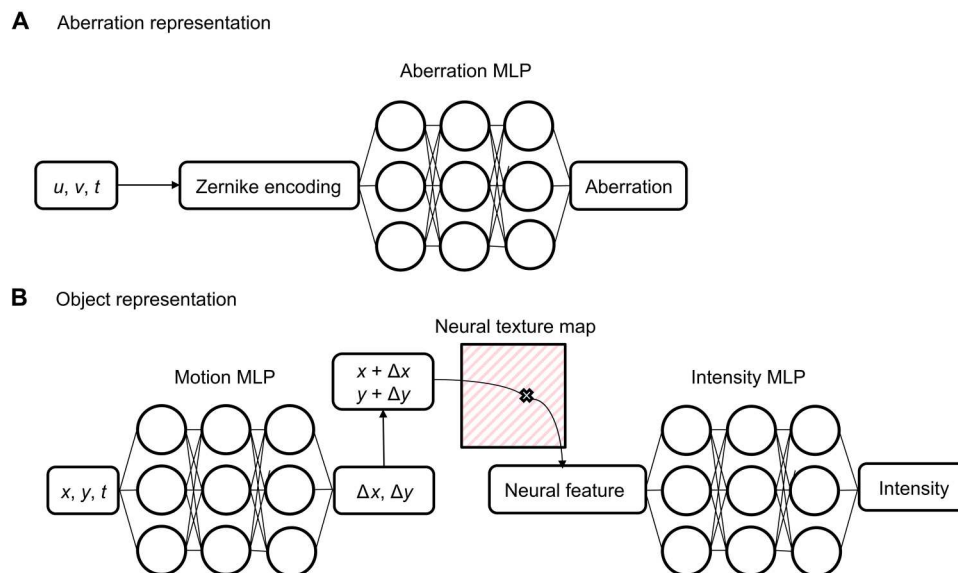


Fig. 6. Network architectures. (A) We use a multilayer perceptron (MLP) network to predict the aberration based on the input (u, v, t) . The standard approach to parameterizing the aberration is through modeling the phase error ϕ , but our setup also allows estimating of the amplitude error. For the input coordinates (u, v, t) , the spatial coordinates (u, v) are first transformed with N_z Zernike basis functions and then concatenated with t . Then, the transformed input is processed by the MLP. (B) We use a combination of two MLP networks and a neural texture map to predict the object based on the input (u, v, t) . Specifically, to handle potential object motions, we use the first MLP network to predict a displacement vector $(\Delta x, \Delta y)$ given the input (x, y, t) . Every time-dependent observation (x, y, t) is then transformed to a stationary canonical space at location $(x + \Delta x, y + \Delta y)$. Then, we sample the neural texture map at $(x + \Delta x, y + \Delta y)$ to obtain a multidimensional vector representing the spatial feature of the canonical coordinate $(x + \Delta x, y + \Delta y)$. Last, we use the second MLP to predict the object intensity based on the sampled feature vector for each coordinate.

MATERIALS AND METHODS

Experimental setup

We created spatially incoherent narrowband illumination by passing light from a 532-nm laser (Z-LASER Z40M18B) through a high-speed rotating diffuser (Thorlabs DDR25, Thorlabs DG10-600-MD) and a laser speckle reducer (Optotune LSR-3005). We used a Holoeye LETO-3 SLM to modulate the wavefront with randomly generated patterns. The patterns were generated by forming weighted sums of the first 15 basis functions of a Zernike polynomial where the weights were determined by sampling from independent Gaussian distributions whose SDs were all 5 radians. Data were captured with a 1384-by-1036 pixel Grasshopper3 complementary metal-oxide semiconductor camera. For the dynamic experiments, motion was introduced with a rotation stage (Thorlabs K10CR1) and a piezo translation stage (Thorlabs Z825B). A detailed diagram of our experimental setup is provided in the Supplementary Materials.

Algorithm

Neural aberration representation

As illustrated in Fig. 6A, we used a multilayer perceptron (MLP) network to predict the aberration ϕ at location (u, v) at time t . To encode the input (u, v, t) , we evaluated the first 28 Zernike basis functions at (u, v) and concatenated the output values with t . The encoded input was then processed by a eight-layer MLP with a hidden dimension size of 32 and leaky rectified linear unit activations. We modeled the aberration ϕ at a resolution of 256 by 256. The number of MLP layers may be tuned for each scene to improve performance.

Neural object representation

As illustrated in Fig. 6B, we used a combination of two MLP networks to predict the object brightness o based on the input (x, y, t) . To handle potential object motion across measurements, we used the first MLP, with three layers and 32 hidden dimensions, to predict a displacement vector $(\Delta x, \Delta y)$ given the input (x, y, t) . Every time-dependent observation (x, y, t) was then transformed to a stationary canonical space at location $(x + \Delta x, y + \Delta y)$. Next, we obtained the canonical space feature of $(x + \Delta x, y + \Delta y)$ by projecting it onto a learnable neural texture map (58). Last, we used the second MLP, with two layers and 32 hidden dimensions, to transform the sampled feature into the predicted object intensity. The neural texture map serves as a flexible point embedding function that mitigates the second MLP's learning burden and allows use to use smaller a MLP and thus train faster without sacrificing representation capacity. We modeled the object o at a resolution of 256 by 256. The number of MLP layers may be tuned for each scene to improve performance.

Optimization

After applying L randomly generated modulation patterns $\Gamma_1, \Gamma_2, \dots, \Gamma_L$ and capturing L different measurements I_1, I_2, \dots, I_L , we performed 1000 epochs of stochastic gradient descent to minimize the negative log-likelihood objective described by Eqs. 2 and 3. Each iteration used a randomly selected batch of four images, and the gradient-based update was performed using the Adam optimizer (59) with a learning rate of 1×10^{-3} .

Supplementary Materials

This PDF file includes:

Legends for movies S1 to S3
Figs. S1 to S13
Tables S1 to S3
References

Other Supplementary Material for this manuscript includes the following:

Movies S1 to S3

REFERENCES AND NOTES

1. A. T. Wiatnik, D. F. Gardner, Wavefront sensing in deep turbulence. *Opt. Photon. News* **29**, 38–45 (2018).
2. S. Yoon, M. Kim, M. Jang, Y. Choi, W. Choi, S. Kang, W. Choi, Deep optical imaging within complex scattering media. *Nat. Rev. Phys.* **2**, 141–158 (2020).
3. S. Gigan, O. Katz, H. B. de Aguiar, E. R. Andresen, A. Aubry, J. Bertolotti, E. Bossy, D. Bouchet, J. Brake, S. Brasselet, Y. Bromberg, H. Cao, T. Chaigne, Z. Cheng, W. Choi, T. Cizmár, M. Cui, V. R. Curtis, H. Defienne, M. Hofer, R. Horisaki, R. Horstmeyer, N. Ji, A. K. LaViolette, J. Mertz, C. Moser, A. P. Mosk, N. C. Pégard, R. Piestun, S. Popoff, D. B. Phillips, D. Psaltis, B. Rahmani, H. Rigneault, S. Rotter, L. Tian, I. M. Vellekoop, L. Waller, L. Wang, T. Weber, S. Xiao, C. Xu, A. Yamilov, C. Yang, H. Yilmaz, Roadmap on wavefront shaping and deep imaging in complex media. *J. Phys. Photonics* **4**, 042501 (2022).
4. M. J. Booth, Adaptive optical microscopy: The ongoing quest for a perfect image. *Light Sci. Appl.* **3**, e165 (2014).
5. K. M. Hampson, R. Turcotte, D. T. Miller, K. Kurokawa, J. R. Males, N. Ji, M. J. Booth, Adaptive optics for high-resolution imaging. *Nat. Rev. Methods Primers* **1**, 68 (2021).
6. J. Wu, Z. Lu, D. Jiang, Y. Guo, H. Qiao, Y. Zhang, T. Zhu, Y. Cai, X. Zhang, K. Zhanghao, H. Xie, T. Yan, G. Zhang, X. Li, Z. Jiang, X. Lin, L. Fang, B. Zhou, P. Xi, J. Fan, L. Yu, Q. Dai, Iterative tomography with digital adaptive optics permits hour-long intravital observation of 3D subcellular dynamics at millisecond scale. *Cell* **184**, 3318–3332.e17 (2021).
7. J. Wu, Y. Guo, C. Deng, A. Zhang, H. Qiao, Z. Lu, J. Xie, L. Fang, Q. Dai, An integrated imaging sensor for aberration-corrected 3D photography. *Nature* **612**, 62–71 (2022).
8. I. M. Vellekoop, A. P. Mosk, Focusing coherent light through opaque strongly scattering media. *Opt. Lett.* **32**, 2309–2311 (2007).
9. A. P. Mosk, A. Lagendijk, G. Leroose, M. Fink, Controlling waves in space and time for imaging and focusing in complex media. *Nat. Photonics* **6**, 283–292 (2012).
10. I. M. Vellekoop, M. Cui, C. Yang, Digital optical phase conjugation of fluorescence in turbid tissue. *Appl. Phys. Lett.* **101**, 081108 (2012).
11. R. Horstmeyer, H. Ruan, C. Yang, Guidestar-assisted wavefront-shaping methods for focusing light into biological tissue. *Nat. Photonics* **9**, 563–571 (2015).
12. D. Aizik, I. Gkioulekas, A. Levin, Fluorescent wavefront shaping using incoherent iterative phase conjugation. *Optica* **9**, 746–754 (2022).
13. P. Lai, L. Wang, J. W. Tay, L. V. Wang, Photoacoustically guided wavefront shaping for enhanced optical focusing in scattering media. *Nat. Photonics* **9**, 126–132 (2015).
14. X. Xu, H. Liu, L. V. Wang, Time-reversed ultrasonically encoded optical focusing into scattering media. *Nat. Photonics* **5**, 154–157 (2011).
15. C.-L. Hsieh, Y. Pu, R. Grange, D. Psaltis, Digital phase conjugation of second harmonic radiation emitted by nanoparticles in turbid media. *Opt. Express* **18**, 12283–12290 (2010).
16. I. N. Papadopoulos, J.-S. Jouhannau, J. F. A. Poulet, B. Judkewitz, Scattering compensation by focus scanning holographic aberration probing (F-SHARP). *Nat. Photonics* **11**, 116–123 (2016).
17. Y. Wu, M. K. Sharma, A. Veeraraghavan, WISH: Wavefront imaging sensor with high resolution. *Light Sci. Appl.* **8**, 44 (2019).
18. A. Thendiyammal, G. Osnabrugge, T. Knop, I. M. Vellekoop, Model-based wavefront shaping microscopy. *Opt. Lett.* **45**, 5101–5104 (2020).
19. J. Bertolotti, E. G. van Putten, C. Blum, A. Lagendijk, W. L. Vos, A. P. Mosk, Non-invasive imaging through opaque scattering layers. *Nature* **491**, 232–234 (2012).
20. O. Katz, P. Heidmann, M. Fink, S. Gigan, Non-invasive single-shot imaging through scattering layers and around corners via speckle correlations. *Nature Photonics* **8**, 784–790 (2014).
21. Y. Sun, Z. Xia, U. S. Kamilov, Efficient and accurate inversion of multiple scattering with deep learning. *Opt. Express* **26**, 14678–14688 (2018).
22. Y. Li, Y. Xue, L. Tian, Deep speckle correlation: A deep learning approach towards scalable imaging through scattering media. *Optica* **5**, 1181–1190 (2018).
23. W.-Y. Chen, M. O'Toole, A. C. Sankaranarayanan, A. Levin, Enhancing speckle statistics for imaging inside scattering media. *Optica* **9**, 1408–1416 (2022).

24. Y. Luo, Y. Zhao, J. Li, E. Çetintaş, Y. Rivenson, M. Jarrahi, A. Ozcan, Computational imaging without a computer: Seeing through random diffusers at the speed of light. *eLight* **2**, 4 (2022).
25. D. B. Conkey, A. N. Brown, A. M. Caravaca-Aguirre, R. Piestun, Genetic algorithm optimization for focusing through turbid media in noisy environments. *Opt. Express* **20**, 4840–4849 (2012).
26. A. Boniface, B. Blochet, J. Dong, S. Gigan, Noninvasive light focusing in scattering media using speckle variance optimization. *Optica* **6**, 1381–1385 (2019).
27. G. Stern, O. Katz, Noninvasive focusing through scattering layers using speckle correlations. *Opt. Lett.* **44**, 143–146 (2019).
28. A. Daniel, D. Oron, Y. Silberberg, Light focusing through scattering media via linear fluorescence variance maximization, and its application for fluorescence imaging. *Opt. Express* **27**, 21778–21786 (2019).
29. T. Yeminy, O. Katz, Guidestar-free image-guided wavefront shaping. *Sci. Adv.* **7**, eabf5364 (2021).
30. M. E. Siemons, N. A. Hanemaaijer, M. H. Kole, L. C. Kapitein, Robust adaptive optics for localization microscopy deep in complex tissue. *Nat. Commun.* **12**, 3407 (2021).
31. R. A. Muller, A. Buffington, Real-time correction of atmospherically degraded telescope images through image sharpening. *J. Opt. Soc. Am.* **64**, 1200–1210 (1974).
32. A. E. Tippie, J. R. Fienup, Phase-error correction for multiple planes using a sharpness metric. *Opt. Lett.* **34**, 701–703 (2009).
33. M. T. Banet, J. R. Fienup, J. D. Schmidt, M. F. Spencer, 3D multi-plane sharpness metric maximization with variable corrective phase screens. *Appl. Optics* **60**, G243–G252 (2021).
34. S. A. Hussain, T. Kubo, N. Hall, D. Gala, K. Hampson, R. Parton, M. A. Phillips, M. Wincott, K. Fujita, I. Davis et al., Wavefront-sensorless adaptive optics with a laser-free spinning disk confocal microscope. *J. Microsc.* **288**, 106–116 (2020).
35. E. J. Candes, X. Li, M. Soltanolkotabi, Phase retrieval from coded diffraction patterns. *Appl. Comput. Harmon. Anal.* **39**, 277–299 (2015).
36. C. Wang, X. Dun, Q. Fu, W. Heidrich, Ultra-high resolution coded wavefront sensor. *Opt. Express* **25**, 13736–13746 (2017).
37. Y. Wu, F. Li, F. Willomitzer, A. Veeraghavan, O. Cossairt, “WISHED: Wavefront Imaging Sensor with High Resolution And Depth Ranging,” in *Proceedings of the 2020 IEEE International Conference on Computational Photography (ICCP)*, 2020, pp. 1–10.
38. V. Sitzmann, J. Martel, A. Bergman, D. Lindell, G. Wetzstein, “Implicit Neural Representations with Periodic Activation Functions,” in *Proceedings of the Conference on Advances in Neural Information Processing Systems (NeurIPS)*, 2020, vol. 33.
39. E. Bostan, R. Heckel, M. Chen, M. Kellman, L. Waller, Deep phase decoder: Self-calibrating phase microscopy with an untrained deep neural network. *Optica* **7**, 559–562 (2020).
40. R. Cao, F. L. Liu, L.-H. Yeh, L. Waller, “Dynamic Structured Illumination Microscopy With a Neural Space-Time Model,” in *Proceedings of the 2022 IEEE International Conference on Computational Photography (ICCP)*, 2022, pp. 1–12.
41. U. S. Kamilov, I. N. Papadopoulos, M. H. Shoreh, A. Goy, C. Vonesch, M. Unser, D. Psaltis, Learning approach to optical tomography. *Optica* **2**, 517–522 (2015).
42. R. Liu, Y. Sun, J. Zhu, L. Tian, U. S. Kamilov, Recovery of continuous 3D refractive index maps from discrete intensity-only measurements using neural fields. *Nat. Mach. Intell.* **4**, 781–791 (2022).
43. J. Yoo, K. H. Jin, H. Gupta, J. Yerly, M. Stuber, M. Unser, Time-dependent deep image prior for dynamic MRI. *IEEE Trans. Med. Imaging* **40**, 3337–3348 (2021).
44. B. Mildenhall, P. P. Srinivasan, M. Tancik, J. T. Barron, R. Ramamoorthi, R. Ng, “NeRF: Representing Scenes as Neural Radiance Fields for View Synthesis,” in *Proceedings of the European Conference on Computer Vision (ECCV)*, 2020.
45. J. J. Park, P. R. Florence, J. Straub, R. A. Newcombe, S. Lovegrove, “DeepSDF: Learning Continuous Signed Distance Functions for Shape Representation,” in *Proceedings of the 2019 IEEE/CVF Conference on Computer Vision and Pattern Recognition (CVPR)*, 2019, pp. 165–174.
46. B. Y. Feng, A. Varshney, “SIGNET: Efficient Neural Representation for Light Fields,” in *Proceedings of the 2021 IEEE/CVF International Conference on Computer Vision (ICCV)*, 2021, pp. 14204–14213.
47. J. Liu, M. M. Balaji, C. A. Metzler, M. S. Asif, P. Rangarajan, Solving inverse problems using self-supervised deep neural nets, in *Computational Optical Sensing and Imaging* (Optica Publishing Group, 2021).
48. E. D. Zhong, T. Bepler, B. Berger, J. H. Davis, CryoDRGN: Reconstruction of heterogeneous cryo-EM structures using neural networks. *Nat. Methods* **18**, 176–185 (2021).
49. E. Dupont, H. Kim, S. M. A. Eslami, D. J. Rezende, D. Rosenbaum, “From Data to Functa: Your Data Point is a Function and You Can Treat It Like One,” in *Proceedings of the 39th International Conference on Machine Learning (PMLR)*, 2022, vol. 162, pp. 5694–5725.
50. B. Y. Feng, S. Jabbireddy, A. Varshney, “VIINTER: View Interpolation with Implicit Neural Representations of Images,” in *Proceedings of the SIGGRAPH Asia 2022 Conference Papers* (2022).
51. M. A. May, N. Barré, K. K. Kummer, M. Kress, M. Ritsch-Marte, A. Jesacher, Fast holographic scattering compensation for deep tissue biological imaging. *Nat. Commun.* **12**, 4340 (2021).
52. M. M. Qureshi, J. Brake, H.-J. Jeon, H. Ruan, Y. Liu, A. M. Safi, T. J. Eom, C. Yang, E. Chung, In vivo study of optical speckle decorrelation time across depths in the mouse brain. *Biomed. Opt. Express* **8**, 4855–4864 (2017).
53. A. P. Wong, B. R. Norris, P. G. Tuthill, R. Scalzo, J. Lozi, S. B. Vievard, O. Guyon, Predictive control for adaptive optics using neural networks. *J. Astron. Telesc. Instrum. Syst.* **7**, 019001 (2021).
54. D. Débarre, E. J. Botcherby, T. Watanabe, S. Srinivas, M. J. Booth, T. Wilson, Image-based adaptive optics for two-photon microscopy. *Opt. Lett.* **34**, 2495–2497 (2009).
55. M. Pircher, R. J. Zawadzki, Review of adaptive optics OCT (AO-OCT): Principles and applications for retinal imaging [Invited]. *Biomed. Opt. Express* **8**, 2536–2562 (2017).
56. S. Kang, P. Kang, S. Jeong, Y. Kwon, T. D. Yang, J. H. Hong, M. Kim, K.-D. Song, J. H. Park, J. H. Lee et al., High-resolution adaptive optical imaging within thick scattering media using closed-loop accumulation of single scattering. *Nat. Commun.* **8**, 2157 (2017).
57. G. Satat, B. Heshmat, D. Raviv, R. Raskar, All photons imaging through volumetric scattering. *Sci. Rep.* **6**, 33946 (2016).
58. E. Chan, C. Z. Lin, M. A. Chan, K. Nagano, B. Pan, S. D. Mello, O. Gallo, L. J. Guibas, J. Tremblay, S. Khamis, T. Karras, G. Wetzstein, “Efficient Geometry-Aware 3D Generative Adversarial Networks,” in *Proceedings of the 2022 IEEE/CVF Conference on Computer Vision and Pattern Recognition (CVPR)*, 2022, pp. 16102–16112.
59. D. P. Kingma, J. Ba, “Adam: A Method for Stochastic Optimization,” in *Proceedings of the International Conference on Learning Representations (ICLR)*, 2015.
60. M. Alterman, C. Bar, I. Gkioulekas, A. Levin, Imaging with local speckle intensity correlations: Theory and practice. *ACM Trans. Graph.* **40**, 1–22 (2021).
61. H. Li, Z. Xu, G. Taylor, C. Studer, T. Goldstein, “Visualizing the Loss Landscape of Neural Nets,” *Advances in Neural Information Processing Systems 31 (NeurIPS)* 2018.

Acknowledgments

Funding: This work was supported by AFOSR Young Investigator Program Award no. FA9550-22-1-0208, NSF CAREER Award no. IIS-1652633, NSF Expeditions Award no. IIS-1730574, NIH DeepDOF RO1 Award no. R01DE032051-01, and NSF PATHS-UP ERC Award no. EEC-1648451. Partial funding for open access was provided by the UMD Libraries’ Open Access Publishing Fund. **Author contributions:** Listed alphabetically. Conceptualization: A.V. and C.A.M. Methodology: B.Y.F. and H.G. Investigation: B.Y.F., H.G., M.K.S., M.X., and V.B. Visualization: B.Y.F., C.A.M., H.G., and M.X. Supervision: A.V. and C.A.M. Writing: A.V., B.Y.F., C.A.M., H.G., M.X., and V.B. **Competing interests:** C.A.M., A.V., B.Y.F., H.G., M.X., V.B., and M.K.S. are inventors on a patent application to be filed by the University of Maryland. The authors declare that they have no other competing interests. **Data and materials availability:** All data needed to evaluate the conclusions in the paper are present in the paper and/or the Supplementary Materials. All data generated during this study are available at <https://doi.org/10.5061/dryad.6t1g1jx42>. The NeuWS source code is available at <https://doi.org/10.528/zenodo.7897446>. Code is also available at <https://github.com/Intelligent-Sensing/NeuWS>.

Submitted 28 December 2022

Accepted 23 May 2023

Published 28 June 2023

10.1126/sciadv.adg4671